Near-infrared spectroscopy of the most powerful black-hole X-ray binary: GRS1915+105

Author: Carlos Martínez Sebastián

Tutors: Dr. T. Muñoz-Darias and J. Sánchez-Sierras

Resumen

Contexto. En la actualidad, el estudio de sistemas binarios de rayos X (compuestos por un objeto compacto, típicamente un agujero negro o una estrella de neutrones, llamado acretor, y una estrella compañera, llamada donante) tiene un gran interés científico por su propia física y su relación con el medio. En particular, aquellos que contienen un agujero negro permiten una mejor comprensión de la física extrema que se da alrededor de estas singularidades. En este campo, los procesos de acreción resultan de interés propio ya que se trata de los procesos más eficientes conocidos a la hora de convertir energía y están relacionados con las inyecciones de energía al medio interestelar (en casos como las binarias de rayos X) o intergaláctico (en casos como los núcleos activos de galaxias o AGNs). Por ello, comprender estos fenómenos es uno de los principales objetivos en la astrofísica moderna. En este sentido, los sistemas binarios con agujeros negros de masa estelar tiene un gran interés, ya que las escalas de tiempo de sus variaciones son menores a aquellas de sistemas más masivos (como los AGNs), permitiendo un estudio de la evolución de los procesos de acreción y sus distintos estados en un mismo sistema, pudiendo comprender mejor la física que los gobierna.
GRS 1915+105 resulta uno de los sistemas binarios de rayos X de baja masa más interesantes y estudiados. Está formado por un agujero negro y una estrella gigante de tipo K. Parte del gas de esta última es acretada, formando un disco de acreción, por el objeto compacto al sobrepasar su lóbulo de Roche. Este sistema, considerado semi-persistente, ha permanecido en outburst, con emisiones cercanas a la luminosidad de Eddington, desde su descubrimiento en 1992 hasta mediados de 2018, cuando se notificó una gran caida en su luminosidad. Sin embargo, en 2019 se observaron inesperados flares en rayos X y radio. Esto llevó a que se propusieran diversas teorías sobre su origen. Una de las más destacadas es la de un inusual estado de oscurecimiento, en que el material circundante absorvería parte de la luminosidad de la fuente, que seguiría siendo intrínsecamente brillante en la longitud de rayos X.
Objetivos. En el presente Trabajo de Final de Máster se realiza un estudio de esta fuente desde una perspectiva multi-frecuencia. Las distintas longitudes de onda permiten analizar distintas partes del sistema. En particular, los rayos X permiten el estudio de la zona más cerca al agujero negro, mientras que el infrarrojo cercano está asociado a una zona relativamente fría del disco de acreción y otras estructuras como el jet. En este proyecto, analizamos la evolución de la fuente en los últimos 5 años, buscando una posible relación entre los rayos X y el infrarrojo cercano. Esto nos permite un estudio del disco en una región distinta a la observada en los últimos tiempos, con lo que pretendemos profundizar en el análisis de los diversos estados de acreción y, al tratarse de una discusión abierta, nos resulta de particular interés el estado actual de la fuente. La combinación de nuestras observaciones en el infrarrojo cercano con la información publicada sobre observaciones en radio y los datos en rayos X, nos permiten entender mejor la física relacionada con este sistema.
Métodos. Este trabajo está basado en medidas espectroscópicas de la fuente en banda $K_{\rm spec}$ (infrarrojo-cercano) obtenidas con EMIR, un espectrógrafo multiobjeto instalado en el GTC, a lo largo de 14 noches distribuidas en 3 campañas (2017B, 2018B y 2021B). Con esto se cubren 3 luminosidades en rayos X (alta luminosidad, decaimiento y un flare durante quiescencia), rango de longitud de onda que estudiamos gracias a los datos públicos del experimento MAXI. Toda esta información es completada por medidas fotométricas tomadas de las imágenes de adquisición de EMIR.
El análisis espectroscópico se centra en la línea de hidrógeno neutro Brγ, la cual es ajustada a través de una función multigaussiana, con dos o tres componentes (dependiendo de si existe o no sobreemisión en el ala azul de la línea). Durante el análisis, se observó que las 14 noches podían ser agrupadas en 6

épocas (E-17, E-18A, E-18B, E-21A, E-21B y E-21C) considerando la similitud de la línea y la cercanía temporal de las observaciones. Esto permitió incrementar la relación señal a ruido (SNR) en todos los casos. Para este mismo fin se aplicó un rebineado a la línea a estudiar.
Resultados. La línea estudiada presenta una gran variabilidad en las distintas épocas consideradas, pero también mantiene rasgos comunes (en particular, en todas ellas se observa un doble pico asociado al disco de acreción, cuya separación entre máximos está relacionada con la distancia de formación de la línea al objeto acretor, siendo una mayor separación característica de una menor distancia). Esto permite ver una clara evolución en la distancia de formación de Brγ, correlacionada con la luminosidad en rayos X. En este análisis presentamos la idea de que la distancia de emisión de la línea está relacionada con el brillo en rayos X a través de la irradiación que sufre el disco disco, provocada por el objeto compacto. También se observa una sobreemisión en el límite azul de la línea en las épocas E-17, E-18A, E-21A y E-21B, lo cual podría estar asociado a un viento en el disco de acreción. Esta idea se ve reforzada al estudiar la velocidad límite del ala, consistente con la de vientos en otros sistemas binarios de este tipo. La información fotométrica, complementaria a la espectroscopía, permite estudiar un exceso de emisión de origen incierto en el continuo infrarrojo durante la primera campaña. Esto podría estar relacionado con componentes distintas al propio disco, como el jet.
Finalmente, las observaciones más recientes (2021B) muestran una emisión de Brγ de una zona relativamente interna del disco, aunque con una evolución consistente con el flare en rayos X reportado. Esto parece ir en contra de la propuesta de un estado intrínsecamente luminoso pero oscurecido, pues el absorvente debería ser interior a la zona de emisión de Brγ (muy cerca del acretor), o de lo contrario esperaríamos que la emisión de dicha línea fuera más externa debido a que el disco respondería a la irradiación (aún sin absorver); es decir, el disco parece verse afectado por la misma luminosidad medida desde la Tierra.

Abstract

Context. Accretion is one of the most important processes that produce energy feedback in both interstellar and intergalactic media. It is still to be completely understood. In that sense, the rapid evolution in X-ray binaries supposes a great opportunity to test our understanding of the mechanisms relevant to accretion. GRS 1915+105 is a well-known low-mass X-ray binary composed of a black hole and a K-type giant star. It has the longest known orbital period for this type of source and it was emitting at high luminosity in X-rays for more than 25 years, supported by its large accretion disk. In mid-2018, the source faced a decay in luminosity that seemed to indicate a new quiescence state. Nonetheless, flare activity in different bands and other unexpected behavior observed from 2019 on, led to the proposal of an internally obscured state caused by a high-density gas around the central engine.
Aim. We want to study the evolution of the accretion state of the source in the last five years, exploring a possible relation between X-ray luminosity and near-infrared (NIR) spectroscopy. We have a special interest in the current state of the source. This extra information provided by this NIR study will be complementary to those already published in X-ray and radio wavelength and will be used to discuss its physical implications. With that, we want to better understand the physics of the disk and, consequently, the present accretion state, still debated by different authors.
Methods. We carried out spectroscopic observations of GRS 1915+105 in the $K_{\rm spec}$ band for 14 nights across three semesters with EMIR. We covered different X-ray luminosities (high X-ray luminosity, decay, quiescence, and flare in quiescence, derived from the MAXI data). We focus our analysis on the Brγ line, which was reproduced with a multi-Gaussian fit. To characterize the evolution of the line, we computed its equivalent width for the different epochs. Finally, we obtained additional information from photometrical data in the NIR.
Results. The Brγ line displayed great variability in the different observed epochs, which was correlated with the X-ray luminosity. We argue that the emission radius of the line is related to the X-ray luminosity through irradiation of the disk. The photometrical information allowed us to discuss a continuum excess in NIR in the first epoch with an uncertain origin. In addition to that, we detected blue emission excesses in four of the six epochs, that we proposed to be disk winds. The last epoch shows Brγ emissions from the inner part of the disk. This is highly consistent with quiescence. For this reason, we argue in favor of a possible scenario dominated by a decline in the accretion rate as the main responsible for the decrease observed in the X-ray light curve. A contribution from internal obscuration is also considered to be possible, but not dominant.

1. Introduction

Black holes (BH), already proposed in Michell (1784) based on Newtonian physics, are the astrophysical systems with the strongest gravitational fields in the universe. For this reason, stellar-mass BHs suppose the best available test to general relativity (Psaltis, 2008). They are the last evolutionary stadium of the most massive stars, result of their core collapse, in which nothing can prevent the formation of a physical singularity due to gravitational attraction. In that sense, there is a maximum mass for neutron stars (NS) to avoid this collapse (Oppenheimer & Volkoff, 1939; Tolman, 1939), which is around $3M_{\odot}$(Kalogera & Baym, 1996). Therefore, those objects whose final mass is over this value should be BHs. These BHs are expected to be relatively common in our galaxy ($10^8 - 10^9$; Brown & Bethe (1994); van den Heuvel (1992)). However, due to their lack of emissions, only a small fraction of them are expected to be detected. In that sense, those in a binary system ($\sim 10^4$; Yungelson et al. (2006)) are more likely to be detectable. Nonetheless, only a small fraction of this number has already been detected. This is because, nowadays, we need to discover them when they are interacting with the surrounding medium.

1.1. X-ray binaries and accretion

Binary stars are systems composed of two stars that are gravitationally bound orbiting around their center of mass. In certain cases, especially in close binaries, this binarity affects their normal evolution, with particular phenomenology as mass exchanges. However, this has shown to be more the norm than the exception (Hettinger et al., 2015; Martynov, 1971; Sana et al., 2012). A particular type of them are X-ray binaries (e.g. Sco X-1 or Her X-1 (Giacconi et al., 1962; Tananbaum et al., 1972)), characterized by being very luminous in X-rays (when they enters into outburst, they are the brightest objects in the night sky in this range of energies). They are formed by a compact object (NS or BH) called the *accretor* and another star called the *donor* or companion star. The emission is produced by material transferred from the donor that is accreted by the compact object. The mass of the donor plays an important role in this process. For this reason, it is typical to distinguish between low-mass (LMXB, whose typical donor is a main sequence star of $M_{\rm d} \lesssim M_{\odot}$) and high-mass X-ray binaries (HMXB, in which we have an O or B star, which are less common and are typically associated with star-forming regions due to the short lifetime of the primary star).

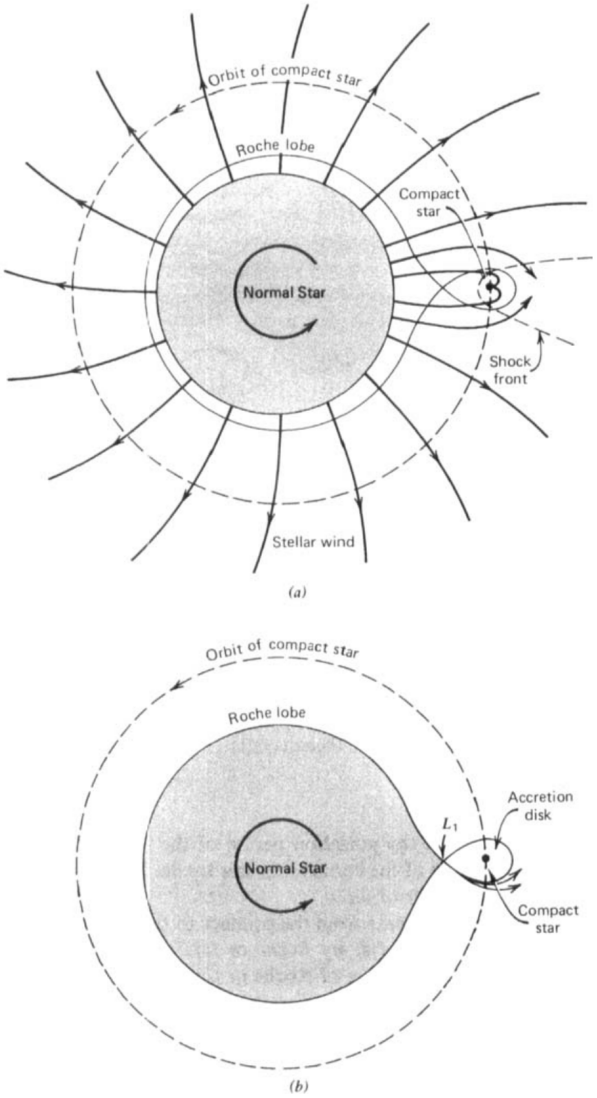

Figure 1: Accretion scenarios in X-ray binaries. The solid curve corresponds to the first common equipotential curve known as the Roche lobe. The dashed line is the orbit of the compact object. **(a)** The donor lies inside its Roche lobe but expels mass via stellar winds, part of which is captured by the accretor. **(b)** The donor is expanded until filling its Roche lobe, and the material begins to overflow through L_1 with a certain angular momentum, forming an accretion disk. *Credit:* Figure 13.11 in Shapiro & Teukolsky (1986)

O and B supergiants present an important mass-loss ($\sim 10^{-6} M_{\odot}\text{year}^{-1}$; Longair (1994)) in the form of winds. In HMXBs, a certain fraction of this material enters the gravitational field of the compact

object and is captured (see (a) panel in Figure 1). As a result, the accretion could be more or less spherical, as the angular momentum of the captured gas may not be sufficient to form a disk. The resulting X-ray luminosity is related to the mass-loss rate of the primary star. This accretion mechanism is relatively inefficient compared to the Roche lobe overflow (see below), as only a part of the expelled material is captured (Eikenberry & Bandyopadhyay, 2000).

In LMXBs, the material is accreted through Roche lobe overflow. The Roche lobe is the first common equipotential surface of each object of the binary (Shapiro & Teukolsky, 1986). It is commonly assumed that the companion star expands and fills its Roche lobe, causing the material to flow through the inner Lagrangian point, L_1 (see panel (b) in Figure 1). In this case, the captured gas has sufficient angular momentum to form a disk around the accretor.

1.1.1. Observational signatures of accretion disks

Accretion is the most efficient energy conversion process known (Longair, 1994). In X-ray binary systems, the matter flowing from the donor to the accretor has a certain angular momentum, which prevents free fall. When the material enters the Roche lobe of the compact object, it starts orbiting around it until encounter the new incoming gas, when the so-called accretion disk is formed. The following material stream hits the disk at a certain point (the hot spot), losing part of its kinetic energy and becoming part of the accretion disk. This structure has observational signatures, such as the double peak when seen at relatively high inclinations (Smak, 1969, it is, when we see the disk close to edge-on). This double peak line profile is characteristic of the accretion disk.

Accretion is able to transfer matter from the outer disk to the accretor. To understand this process, we assume a keplerian, stationary, and geometrically thin accretion disk described in Shakura & Sunyaev (1973). This disk is formed of rings orbiting at different velocities and with different physical characteristics (temperature, density, viscosity, etc.). To fall into the accretor, the matter that composes the disk should lose its angular momentum, which is done by viscous forces. It allows angular momentum to be transferred outwards, and matter to spiral inwards. It is interesting to note that this model is independent of the details of the viscosity mechanism (reason for which we are not discussing it) and uses the phenomenological viscosity parameter, α, prescription (see Shakura & Sunyaev, 1973). This α value is not constant but increases with the surface density.

Further to the ideal model, the disk can present instabilities, mainly associated with hydrogen ionization and radiation pressure. According to their long-term behavior, we can distinguish between persistent and transient sources. At the moment, all known persistent sources containing BHs are HMXBs, while all known BH LMXBs are transient (Done et al., 2007). The latter produces sporadic outbursts, in which their X-ray luminosity increases by several orders of magnitude (despite spending most of their lives in low luminosity states or quiescence, due to the low mass transfer rate from the companion that does not support a permanently ionized disk).

For transient sources in quiescence, we consider there is a more or less constant matter flow inward, with a greater input to each ring than output to the contiguous. This results in an increase in the surface density. When this is over a critical value for a given ring, its viscosity increases, resulting in a more efficient angular momentum loss and, consequently, more material going to the immediately inner ring (it increases its output flux). As the contiguous sections receive a greater input of gas, their density starts to increase rapidly until reaching their critical values. Globally, it produces an avalanche that significantly increases the accretion rate and luminosity of the source. Finally, after having accreted a significant fraction of the disk, the surface density decreases sufficiently, resulting in a decrease of α and the return to quiescence. The distinction between persistent and transient sources is purely observational, without modelling predictions.

This recurrent process produces variations in the spectra, which can be followed through the color (the flux ratio between a hard and a soft energy band, also measured by the hardness). The X-ray spectrum of a LMXB is mainly composed of two components. Firstly, we have a soft component from a thermal emission from the accretion disk[1], composed of the emission of the different rings at different temperatures, which increases inward (Dotani

[1]Note that this requires a thermalized disk, for which it should be optically thick. This is assumed in the Shakura–Sunyaev model. The optically thin disk would produce a two-temperature plasma dominated by Comptonization, bremsstrahlung, and cyclo-synchrotron rather than blackbody radiation (Narayan & Yi, 1995).

et al., 1997; Shakura & Sunyaev, 1973). Note at this point that, as the disk is thermally stratified, when observing at longer wavelengths (e.g., NIR) we are looking at more external parts of this structure. The other is an exponential component probably produced by inverse-Compton processes from the corona (Gilfanov, 2010).

There are different accretion states (Miyamoto et al., 1992, 1993) that produce various X-ray hardness, that follow a characteristic pattern in different systems (Fender et al., 2004). The above-explained outburst produces variations between those regimes as follows (Miyamoto et al., 1995). In the beginning, there is a fast rise in luminosity at (more or less) constant color, that is dominated by high energy emission (the 'hard state'), in which the disk temperature is relatively low. In this case, the inner region is optically thin (and non-thermalized), producing an important Comptonized component (see bottom schemes of Figure 2). After it, there is a transition from a hard to a soft state (lower color) at approximately constant luminosity. In this state, the inner rings are geometrically thick and optically thin (see top schema in Figure 2), and produce a thermal component as well (there is a significant drop in hard X-rays). Finally, the luminosity gradually decreases, to give rise to a soft to hard transition and a final decrease to quiescence. If we follow up on an outburst and plot it in a hardness-intensity diagram, we would obtain a characteristic "Q" shape[2] (Muñoz-Darias et al., 2013).

Depending on the state, these sources also have an important radio emission due to the presence of jets. Jets are highly relativistic, collimated, and powerful outflows (Fender & Belloni, 2004). This complexity arises from the magnetic field. They are usually produced by accelerating the inner part of the disk and corona to relativistic speeds, and they are ejected as synchrotron-emitting plasma (Dhawan et al., 2000). They are very important as kinetic feedback to the interstellar medium, considering the high speed of the launched material. Jets are visible in most of the sources during hard states but quenched when they are softer (Fender et al., 2004). It points to an important disk-jet coupling (Fender & Belloni, 2004; Klein-Wolt et al., 2002).

In addition to jets, disk winds can also result in mass ejections out of the gravitational potential of the compact object. They become very important at a high mass accretion rate, and different physical origins are proposed to drive them (radiation pressure, line driven, thermally driven, or magnetically driven). For a more detailed description of them, we refer the reader to Fender & Muñoz-Darias (2016) and references therein.

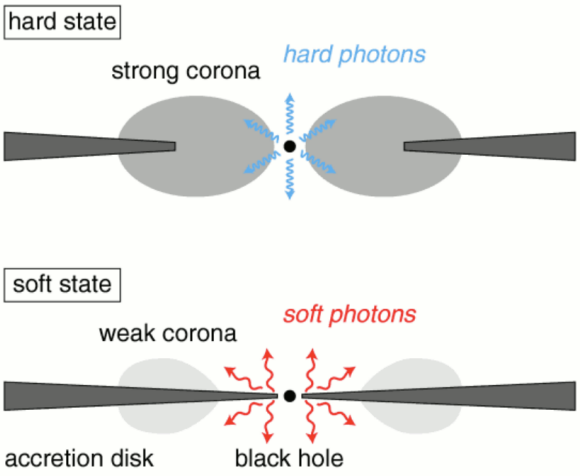

Figure 2: Proposed accretion geometry that explains the two main X-ray spectra observed in X-ray binaries. **Hard state:** There is a contribution in hard X-ray due to Comptonization with the prominent corona. The jet is visible on the radio, but no disk winds are expected. **Soft state:** Mostly the only contribution is from the thermalized disk, resulting in soft X-rays and disk winds. *Credit:* Adaptation of Figure 2 in Liu & Taam (2009)

Stellar-mass BHs seem to display the same inflow-outflow behavior, but in shorter time scales, than Active Galactic Nuclei (AGN; Fender & Belloni (2004)), that have supermassive BHs (SMBHs) accreting at a high rate. For this reason, there have been efforts in recent times to extend the LMXB schema of accretion to AGN. However, the complex phenomenology observed in AGN makes this task difficult (Fernández-Ontiveros & Muñoz-Darias, 2021). Classically, Seyfert galaxies (Seyfert, 1943) have been divided into types 1 and 2 depending, respectively, on the presence or absence of broad permitted emission-line transitions in their optical spectra. Antonucci (1993) proposed a Unified Model, in which this observational difference depends on the observational angle. In that sense, Seyfert 1

[2]In addition to those two basic states depending on X-ray hardness, there are other states (e.g. ultrasoft, very high, etc.) that we are not discussing here. We refer the reader to Belloni (2010) and references therein for further discussion.

are thought to be observed at a low inclination angle, allowing the detection of broad line emissions surrounding the accretion disk. On the other hand, Seyfert 2 are thought to be observed at a high inclination, being affected by a great absorption from a dust torus surrounding the central engine. This torus would have an inner radius ranging from 0.1 to 10 pc Burtscher et al. (2013).

1.2. GRS 1915+105

GRS 1915+105 was discovered by *WATCH* in 1992 (Castro-Tirado et al., 1992) as a transient source with remarkable variability (Castro-Tirado et al., 1994). After this, its counterparts were discovered at higher energies (20-230 keV; Harmon et al. (1992)), radio (Mirabel et al., 1993a), and infrared (Mirabel et al., 1993b) wavelengths. It was the first galactic source in which clear examples of highly relativistic jets were observed. These jets were so relevant, that the term "microquasar" was coined to describe this system (Mirabel & Rodríguez, 1994). It is estimated to be at a distance of $d = 8.6^{+2.0}_{-1.6}$kpc (Reid et al., 2014), and it is known to be greatly affected by interstellar absorption ($N_{\rm H} \sim 2\times10^{22} - 6\times10^{22}{\rm cm}^{-2}$; Belloni et al., 2000). This source has become very famous for several reasons, such as its long outburst (more than 25 years), its particular behavior, and its large accretion disk (Fender & Belloni, 2004).

The accretor is a BH of mass $M_{\rm BH} = 12.4^{+2.0}_{-1.8} M_\odot$ (Reid et al., 2014). The donor is a K-type giant star (Greiner et al., 2001) of 0.3-1$M_\odot$(Steeghs et al., 2013; Ziółkowski & Zdziarski, 2017). Among all-known LMXBs, it has the longest orbital period ($P = 33.85 \pm 0.16$ days; Steeghs et al., 2013), and consequently with the largest accretion disk ($\sim 3\times10^{12}$cm; Truss & Done, 2006). We view this disk at a high inclination (Mirabel & Rodríguez, 1994), with a visual angle of $\theta = 66 \pm 2°$ (Fender et al., 1999). This high inclination favors the possible detection of winds (Fender & Muñoz-Darias, 2016).

Since its discovery in 1992, the system has been in continuous outburst for more than 25 years (Harmon et al., 1997). So was the case, that it was even discussed if it should be considered a persistent source rather than transient (Corral-Santana et al., 2016). It exhibited rich and varied light curves and spectra, which made it possible to deeply discuss the disk-jet coupling of the system (Fender & Belloni 2004; Neilsen & Lee 2009) and its variability. During this long outburst, GRS 1915+105 never reached the low luminosity-hard state (Belloni, 2010). Observationally, it repeated a cycle in the high luminosity-low hardness part of the hardness-intensity diagram (see Figure 3). There were classified three luminosity states (Belloni et al., 1997, 2000) (called A, B, and C, similar to very high and intermediate states in other X-ray binaries; Fender & Belloni (2004)) and multiple classes. By convention, this particular classification persisted for years, despite its anomaly.

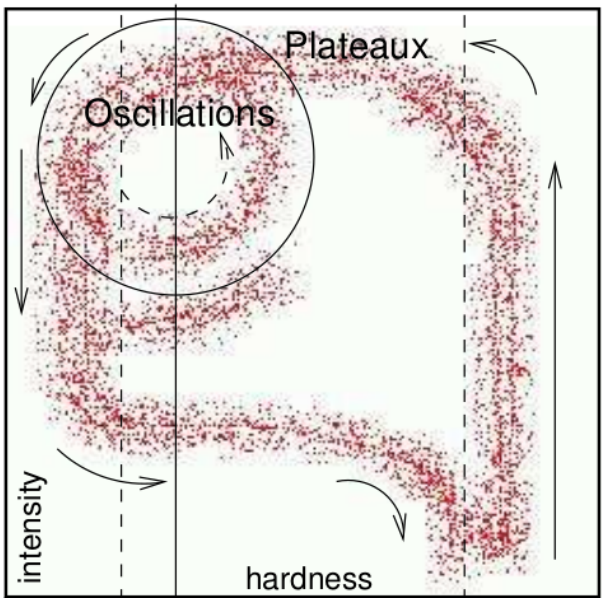

Figure 3: Example of the evolution of outbursts following the color-intensity diagram explained in the text. Typical outbursts follow the solid arrow in an anticlockwise evolution resulting in the characteristic "Q" form. However, GRS 1915+105 appears to be usually in the upper left region of the corner, repeatedly going in the same cycle that crosses the critical limit between producing or not a jet, causing radio flares. *Credit:* Adapted from Figure 27 in Fender & Belloni (2004)

Fender & Belloni (2004) proposed an evolution in accretion that explains the appearance and disappearance of jet detection. Observationally, the hardest phases showed jets, while the softest did not. There was proposed a transition between those phases at a critical color, which was thought to correspond to the geometrically thin disk reaching the innermost stable orbits and, consequently, near the peak in soft X-ray flux. The evolution can be understood as follows: above a certain hardness, there was a jet correlated with X-ray (Corbel et al., 2003). The velocity of the

jet increased when approaching the critical color from hard states, and when it was very close, the jet velocity increased very rapidly, producing a shock in the previously expelled material and finishing with the shut off of the jet. Then, below the critical hardness, the jet was not produced.

Winds have been observed several times in GRS 1915+105. As in other LMXBs, the mechanism that produces them is not clear. In fact, several mechanisms can play a role (Neilsen & Lee, 2009), but thermal winds (Begelman et al., 1983) are thought to be one of the most important. In this particular mechanism, the outer disk is heated due to strong irradiation. This increases the thermal pressure, providing the extra energy necessary to drive the wind off the accretion disk. This mechanism can be suppressed during the hard state, when the inner accretion disk is optically thick, avoiding such effective irradiation in the outer parts. A schematic idea of this mechanism can be seen in Figure 4. Also, winds have been proposed to play a key role in jet suppression, halting the flow of matter into the radio jet (Neilsen & Lee, 2009).

After more than 25 years following this characteristic behavior, finally, in mid-2018, GRS 1915+105

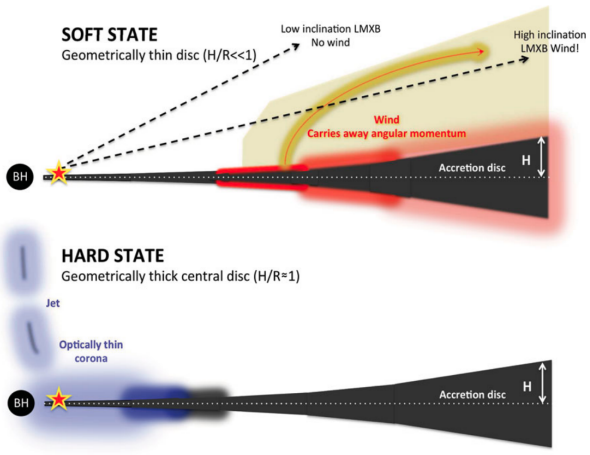

Figure 4: Sketch of the thermal wind mechanism. **Top:** Soft state. The inner disk is geometrically thin, the outer disk is heated, increasing the thermal pressure and forming a wind, which is flattened above the disk. This would be the reason why we only see winds in high inclination sources. **Bottom:** Hard state. The inner disk is geometrically thick and optically thin. There is a corona and a jet, but no winds or little. *Credit:* Figure 3 in Ponti et al. (2012)

entered an unusual low-flux state (Negoro et al., 2018) that could have indicated the beginning of the end of its long outburst started in 1992. However, shortly after this alert, in 2019, it showed unexpected behaviors (Homan et al., 2019a) and radio and X-ray flares were observed with different instruments (Homan et al., 2019b; Iwakiri et al., 2019a,b; Trushkin et al., 2019). In other binary systems, epochs of strong, variable local absorption have been associated with flaring activity (Hare et al., 2020; Muñoz-Darias et al., 2020; Walton et al., 2017). This led to some recent articles that have proposed that GRS 1915+105 may be in an intrinsically obscured state since MJD $\sim$ 58600 (Athulya et al., 2022; Balakrishnan et al., 2021; Koljonen & Tomsick, 2020; Miller et al., 2020; Motta et al., 2021; Neilsen et al., 2020), with values of internal obscuration of $N_{\rm H} \geq 10^{23}{\rm cm}^{-2}$. This would be similar to a Seyfert-2 galaxy, according to Miller et al. (2020). On the other hand, Motta et al. (2021) argued that the expected variability time scales for stellar-mass scaled AGN would be shorter than the observed in GRS 1915+105. In this scenario, despite the fact of observing a low fraction of the Eddington luminosity (this is the maximum luminosity such as the associated radiation pressure does not blow away the infalling matter; Longair, 1994), GRS 1915+105 would be intrinsically not far from this limit (Neilsen et al., 2020). For this to be possible, different intrinsic obscuration scenarios have been proposed, from failed winds in a Seyfert 2-like binary system (Miller et al., 2020) to a vertically extended outer disk (Neilsen et al., 2020).

In this project, we aim to study the evolution of the source using NIR spectroscopy in the period 2017-2021, with a special interest in the open discussion concerning the current state. For that, we carry out a study of the Brγ emission line in six different epochs observed during three different semesters (2017B, 2018B, and 2021B), covering a variety of X-ray luminosities (outburst, decay, and flare in quiescence). The observations used and the data reduction are presented in Section 2. We study the evolution of the line, its shape, and compare it with the X-ray light curve in Section 3. A discussion of the physical implications of these results, complemented with additional information obtained from a variable blue emission of the line and a photometric analysis is performed in Section 4. Finally, the main results of this work, its relevance, and possible further steps for future studies are summarized in Section 5.

2. Observations

2.1. Near-infrared spectroscopy

We carried out spectroscopic observations with EMIR. This is a multi-object infrared spectrograph ($0.9 - 2.5\ \mu$m) optimized for the K band ($\sim 2.1\mu$m). It is installed in the Nasmyth-A focal station of the Gran Telescopio Canarias (GTC). We observed during three different GTC semesters (2017B, 2018A, 2021A) on 14 nights with EMIR. We used a long slit configuration with the $K_{\rm spec}$ filter (see Figure 10), carrying out observations with nodding following an ABBA sequence and RAMP readout mode. The exposure times for the spectroscopic observations ranged from 120s to 200s. We got intermediate-resolution spectra ($R = 4000$ for the used K pseudo-grism without binning). No imaging was requested, but the acquisition images were used to study the photometric variability when possible.

We performed the data reduction with the EMIR data reduction pipeline, `PyEmir`, following the *Spectroscopic mode tutorial: MOS data*. The used calibration files (master flats, master dark, and master bias) are those provided by GTC, regarding the higher number of observations they used, which results in better statistics. The next explained steps were repeated for the data of each observation night, changing the corresponding files according to the information in the tutorial (above in this paragraph).

Firstly, we had to consider the geometric distortions in the raw spectroscopic data. They are modelled, and so are the wavelength calibrations, for any configuration of the CSU. It allowed a preliminary calibration, to be refined later, without needing any additional measure. As a result, we obtained images with wavelength calibration, bad pixels masked, and corrected from dark current, bias, and flat-field. In our case, after the preliminary approach, in which we filtered the slits to be in a certain width range, we worked on a more refined calibration directly with the scientific images (using airglow OH lines). This meant we had calibration references in all images, resulting in a subpixel precision. The offsets in pixels in both spatial and spectroscopic directions, which have to be corrected to improve the current calibration at this step, were estimated by overplotting the expected location of both frontiers (separation between apertures in the CSU) and the brightest expected OH lines over the image to correct. This step was independently done for the different observations we had in order to get better results than using the same values for all. As a result, we get a better calibrated and corrected image. Although an automatic determination of the offsets is possible, it was not used for this project, due to the quality of the other method and the low enough number of observations that makes unnecessary an automatic method.

The next step was the combination of each observation sequence, ABBA. It resulted in pixel-to-pixel background subtraction. Before this, it is usually useful to correct possible offsets of all the A images between them, and the same for all the B images. Hereinafter, we have a two-step process. In the first place, we compute the A spectra minus the B spectra. It produced a double signal of the source (positive and negative signal), but a reduced and flatter background (compare Figure 5a and Figure 5b). Next, we calculate the offset between A and B spectra. Then, we coadd AB files moving the distance of the offset in the spatial direction. The result is a triple spectrum of the source (see Figure 5c): two positives in the extremes (corresponding to the B spectra of the original previous file and the A spectra of the shifted version) and one negative (which contains the sum of the observations from different telescope positions). After this process, we had increased significantly the signal-to-noise ratio (SNR) by adding the signal of the 4 observations and doing a direct subtraction of the background.

The following steps are done using `Python` and other facilities. The programs can be consulted by clicking here. The first thing to do is to extract the 1D spectra (intensity against wavelength) of the source from the combined ABBA images. To do so, we combined several rows of pixels corresponding to our source and extracted all columns of it. This contained extra empty pixels, which were removed. The same process was repeated for the errors. Finally, all observations corresponding to the same night were also coadded to increase the SNR. These results (one spectrum and its error per image) in conjunction with their fits header were saved into new fits files.

Despite having the spectra reduced, they were not corrected from telluric lines yet. This particular surpassed the purpose of this work. Consequently, the spectra were corrected from atmospheric absorption features by the supervisor Javier Sánchez-Sierras, who is experienced with `Molecfit` (Kausch et al., 2015; Smette et al., 2015). This software fits synthetic transmission spectra to astronomical data to

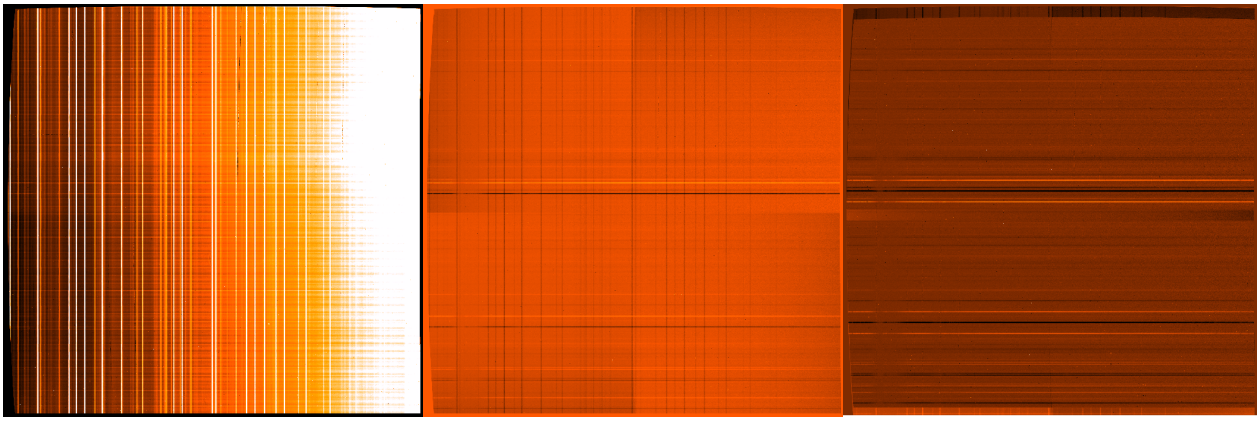

(a) (b) (c)

Figure 5: Example images of the results at different reduction stages for the spectroscopic observations of 25-08-2021. In all three, the X-axis corresponds to the spectral direction, while the Y-axis corresponds to the spatial direction. **Left:** Spectrum in the A position, already wavelength calibrated and corrected from geometrical distortion. Note the important bright gradient in the spectral direction. **Center:** Intermediate step. The spectroscopic file corresponds to B minus A position images. Note that most of the ubiquitous vertical lines (corresponding to bright OH airglow) are masked. There is a remarkable reduction in the background level, and the spectra of different sources are now clear and double, with one positive (above) and one negative (below) signal of each. **Right:** Result of the combination of an ABBA series. After computing the offset between A and B positions, all the A and B spectra are added, producing a triple signal from each source: two positives (white) in the extremes, and one negative (black) in the center. The background subtraction has improved compared to the simple A-B combination (without this extra addition).

correct the absorptions from the terrestrial atmosphere molecules. The further analysis was carried out with `molly`, a specialized tool oriented for astronomical spectra. We grouped the 14 spectra in six epochs, responding to two main criteria. Firstly, the different spectra of the same epoch should correspond to similar X-ray luminosities. Secondly, each individual spectra should be similar enough to the mean spectrum of the group (which is studied). With this criteria, we obtained 1 epoch from semester 2017B, 2 from semester 2018B, and 3 from semester 2021B called E-17, E-18A, E-18B, E-21A, E-21B, and E-21C, respectively. The similarity and validity of the final groups, as well as the representativeness of the average spectra used, and the convenience of the use of average spectra, can be consulted in Figure 9 in Appendix.

2.2. Near-infrared photometry

We performed a photometrical study using the different acquisition images of the observations with EMIR, and we analyzed them with `Astropy` package and functions based on it and created for this project. We created and used our own master flat to reduce the acquisition images. As we did not request photometric images, we did not have flat observations. However, we used those available corresponding to different projects already in the GTC database that were observed using the same filter. To avoid biasing our master flat, we compared flats of different epochs to ensure their similarity. We did not perform bias correction. However, it can be considered as part of the background. Despite the fact of not having the ABBA pattern to do a pixel-to-pixel subtraction, we estimated the background of each source using a ring around it with an inner radius of 2 times the seeing and an area equal to the integrated area of the star. With this, we have an estimation of the background affecting the source without contributions to it (it is significantly separated). This also limited the selection of the reference sources, as they should be isolated to avoid contributions of neighbored sources. The non-detection of the system, non-solved inconsistencies of the results, or the limiting position of the target close to the detector edge (with the subsequent effect over the measured flux) forced us to reject many images to ensure the quality of the photometry.

2.3. X-ray monitoring

For the X-ray study, we used data from the Monitor of All-sky X-ray Image (MAXI), a high-energy astrophysical experiment placed on the Japanese Experiment Module Exposed Facility on the International Space Stations (ISS) (Matsuoka et al., 2009). This instrument started observations in August 2009 and has been monitoring all the X-ray sky since then, producing light curves in ranges of 2-20 keV, 2-4 keV, 4-10 keV, and 10-20 keV with different time bins. Their data are public and can be accessed through this page. We use the light curve in the 2-20 keV range to determine the X-ray luminosity during our campaigns, with a time bin of one day. We note the lack of sensitivity to time-scales lower than that (e.g., heartbeats (Neilsen et al., 2011; Taam et al., 1997) and other rapidly-changing classes in Belloni et al. (2000)). In the top-left panel of Figure 6, we find that our three campaigns correspond to a bright outburst near the maximum, an exponential decay to quiescence near the minimum, and a flare during the low X-ray luminosity (the proposed "obscured" state). This diversity gives us the versatility to better understand the physical processes of the source.

3. Analysis and results

We centered our study in the Brγ line (transition between levels $n = 7$ and $n = 4$ in HI, $\lambda_{\mathrm{vac,Br}\gamma} = 21661.18$ Å; Chang & Deming (1996)). For it, we fitted the line (which always showed the characteristic double-peaked profile; Smak (1969) and a variable excess in the blue wing). We studied their evolution and computed the equivalent width (EW). This is the width that should have a rectangle of height 1 to have the same area as the line. We did not detect any line around $\lambda_{\mathrm{vac}} = 21885$ Å (see Figure 9), which would be associated with He II. Our analysis was completed with photometry when possible.

3.1. Spectroscopy

The spectral analysis was mainly done using `molly` package (by Prof. T.R.Marsh) and `Python`. Previous to that, a visualization of the spectra was done. We detected that those corresponding to the 2021A campaign showed a narrow absorption close to the red limit of the line, probably associated with a non-perfect subtraction of a telluric line of CH_4. As its origin is not in the target, we masked this feature by interpolating the continuum, to avoid spurious effects in the analysis. Next, we created the average spectra of the groups with `molly`, trimmed them in a wavelength range around Brγ (21106 Å-22210 Å), and normalized their continuum. For the latter, we fitted the continuum with a polynomial of degree two and divided the segment of the spectra by it. Finally, we rebinned the line to increase the SNR. In epochs E-17, E-18A, E-21A, and E-21B, we used a binning of two pixels, while for E-18B and E-21C, due to the higher noise level, we decided to use a binning of 5 pixels (see the second column in Table 1). With that, we ensured a SNR over 4 in the continuum in all cases (see the third column in Table 1). From this point on, we used these trimmed rebinned Brγ-centered spectra for our study. As the project was based on a particular line and in order to facilitate their physical interpretation, we opted for using velocities centered in $\lambda_{\mathrm{vac,Br}\gamma}$ instead of wavelength to work with the spectra. The conversion is regulated by

$$v = \frac{\lambda - \lambda_{\mathrm{vac,Br}\gamma}}{\lambda_{\mathrm{vac,Br}\gamma}} c, \tag{1}$$

where λ is the corresponding observed wavelength. Consequently, from now on we are generally talking about velocities referred to at the center of the line at rest.

Epoch[(a)]	Binned [km/s][(b)]	SNR[(c)]
17	47.9	7.1
18A	47.9	9.5
18B	119.75	4.2
21A	47.9	6.8
21B	47.9	11.3
21C	119.75	5.1

Table 1: Summary of NIR epochs characteristics. [(a)]Name of the epoch. [(b)]Pixel size used in the study (after rebinning) in km/s. [(c)]Computed signal-to-noise ratio for the used binning.

The EW is here to measure the strength of the line, with the advantages of being independent of the specific resolution and intrinsic broadening. It was integrated with `molly` using a broad mask (-1535 km/s to 540 km/s) to include all the important features of the line (double peak and blue excess, when present) while limiting the continuum. With this, we took into account the complex variability of the line, including the blue edge. However, as the limit of the blue wing

change depending on the epoch (including the non-detection of this, see Table 3), the proportion of noisy continuum changes as well. In Figure 6, we can see a summary of the observations of this work. There is different complexity in the lines (with an emission excess in the blue wing in some cases) and a great variability considering all the six epochs. We can see that the results from EW are consistent with what we would expect by looking at the line spectra of the epochs (right panels of the Figure).

E-17 corresponds to high X-ray luminosity during the outburst. However, the equivalent width of Brγ is close to the minimum (5.45 ± 0.13 Å). The line shows a prominent blue component and a double peak with one of the lowest separations.

E-18A and E-18B were observed at the end of a very prominent X-ray luminosity decay, after which the system entered a long quiescence period (Koljonen & Hovatta, 2021). In fact, X-ray luminosity during E-18B is already consistent with quiescence. The EW in E-18A is almost a factor two larger than in the other epochs (10.93 ± 0.24 Å). After 11 days (separation between the last observation of E-18A and the first observation of E-18B) the EW decreases to half of its previous measured value (5.43 ± 0.38 Å) and is comparable to E-17. The evolution of the line shows important variations between these two epochs (higher intensity with a lower double peak separation and important blue excess in the former versus more markedly separated lower intensity without any obvious excess in the blue wing in the latter). However, the lower SNR in E-18B (see Table 1) could result in the unlikely hiding of a real blue component under the noise level. These spectra have an especial interest as they are consistent with a low luminosity level in X-ray close to quiescence, not before observed in GRS 1915+105.

Finally, the three spectra studied in 2021 correspond to a flare at low luminosity. The equivalent width of all of them are quite similar (6.40 ± 0.26 Å, 6.79 ± 0.19 Å, and 5.85 ± 0.39 Å respectively), with a slightly lower value in E-21C, but far from the variation between E-18A and E-18B. The Brγ line shows remarkable variations. From E-21A to E-21B, there is a decrease in the separation of the double peak but an increase in the line intensity. In both cases, we have a clear contribution of a blue excess. Nonetheless, E-21C does not show any extra contribution in the blue wing, the separation between the double peak is higher, and its intensity is lower (comparable to E-21A or E-18B).

3.1.1. Line profile fitting

To fit the line, we used the function `curve_fit` from `scipy.optimize` package in Python. It uses non-linear least square optimization to fit a function, f, to data, returning the optimal values of the parameters as well as the estimated covariance matrix, where the diagonal corresponds to the covariance of the parameters, which can be used to estimate their errors. To reproduce each line, we assume a double peak composed of two Gaussian with the same full width at half maximum (FWHM), and then we used the same standard deviation, σ, for both. An additional component with a different standard deviation was included in E-17, E-18A, E-21A, and E-21B (when an additional blue emission component was observed). Explicitly, the general mathematical form used to fit the line is

$$1 + A_1 e^{\frac{-(x-\mu_1)^2}{2\sigma^2}} + A_2 e^{\frac{-(x-\mu_2)^2}{2\sigma^2}} + A_b e^{\frac{-(x-\mu_b)^2}{2\sigma_b^2}}, \quad (2)$$

where the last term corresponds to the blue excess. This term is removed when it is not present. For the cases in which the last component is necessary, we did a first fit with only two components, fitting the double peak as a single Gaussian and the blue emission as a different one. It allowed fixing lately the parameters of the blueshifted distribution in order to only have to minimize 5 parameters in each case. To better estimate the error, we used the Montecarlo (MC) method with 10000 steps, changing the initial conditions randomly within certain ranges of values to avoid any dependency of the fit with them. We rejected those fits without physical meaning. The final values selected correspond to the median of each parameter, while the associated error was the maximum between the square root of the covariance and the standard deviation of the distribution of fitted parameters with the MC method. Finally, we also include a fitting of the line as a single Gaussian to study its global evolution (i.e. shifting in the center of the line).

Figure 7 shows Brγ lines of the different epochs (same colors as in Figure 6) and the corresponding fittings (in solid blue for the total and dashed blue for the individual components). Vertical dotted blue lines mark the end of the spectral line when there is an extended wing. The line evolution display similar behavior between different epochs (see Section 4). We see with special interest the highly consistent

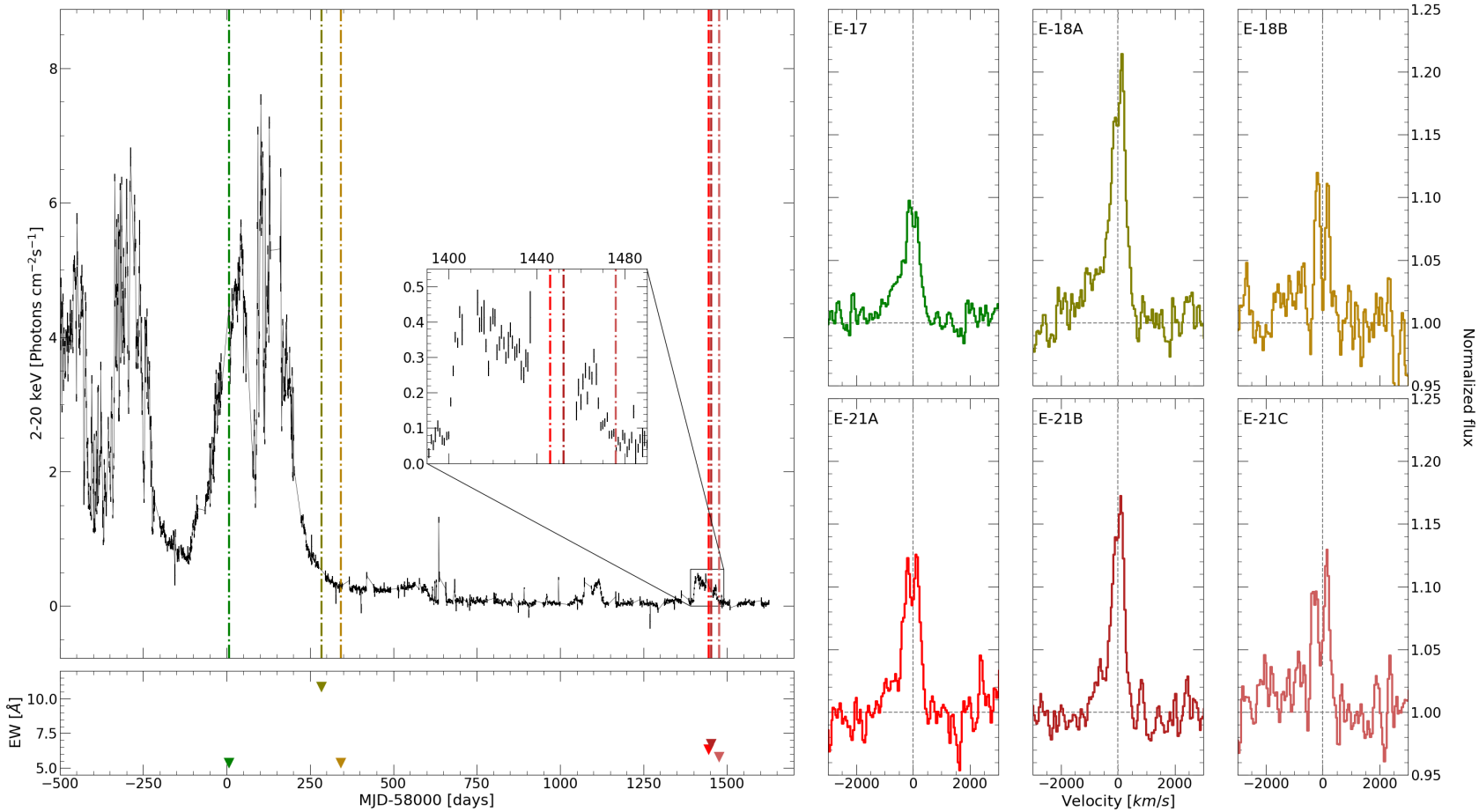

Figure 6: Summary of the observations. The figure is mainly divided into two halves (left, with the first column of panels, and right, containing the remaining three columns). *Top left:* Light curve in X-ray range 2-20 keV for GRS 1915+105 from MAXI. Vertical lines mark the mean observation days of each epoch. The color code corresponds to the color used in the spectra. The inset panel corresponds to zooming over the 2021 flare. *Bottom left:* Equivalent Width of the corresponding average spectra of each epoch. **Right:** Average spectrum of different epochs as a function of the velocity with respect to the wavelength of Brγ in a rest frame of reference. The lines are Gaussian smoothing to stand out the most important features.

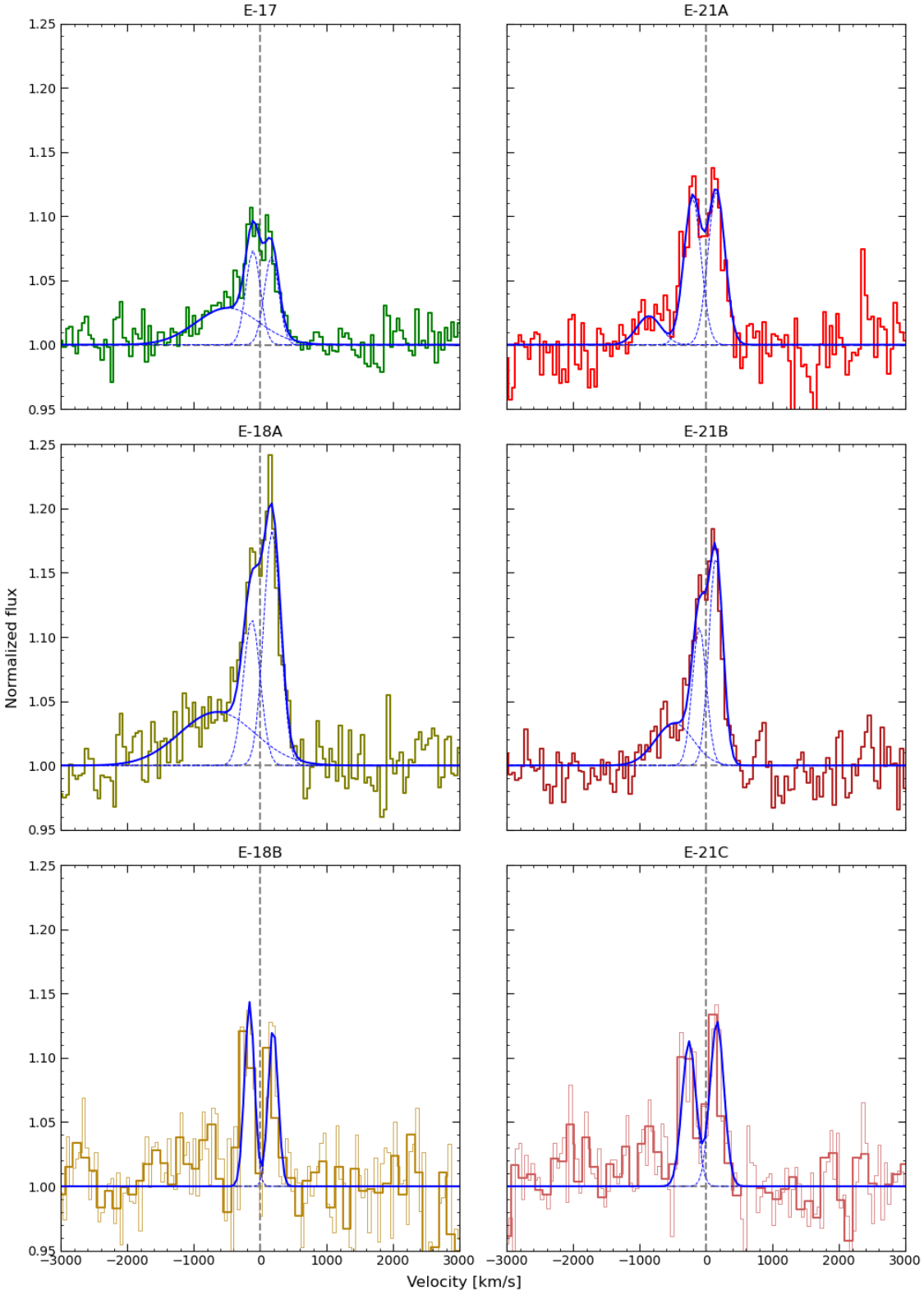

Figure 7: Average spectra of the Brγ line for the six studied epochs (with the same colors as in Figure 6) and the resulting fit. The different fitted components are marked as dashed blue traces. The resulting fitting line for each epoch is in solid blue line. The vertical dotted lines in epochs with marked blue wings correspond to the terminal velocity. Epochs E-18B and E-21C have a greater binning size to increase their SNR, but for comparison, the same binning as in the other epochs is plotted with narrower lines. From top to bottom and left to right, epochs E-17, E-18A, E-18B, E-21A, E-21B, and E-21C.

Epoch[a]	K mag[b]	EW [Å][c]	μ_{DP} [km/s][d]	μ_T [km/s][e]	FWHM$_{DP}$ [km/s][f]	FWHM$_T$ [km/s][g]	Blue edge [km/s][h]	Red edge [km/s][i]	$\Delta\mu_{DP}$ [km/s][j]
17	14.90 ± 0.10	5.5±0.2	31 ± 21	−64 ± 20	520 ± 39	762 ± 20	−1921 ± 297	498 ± 32	278 ± 21
18A	14.53 ± 0.12	10.9±0.3	26 ± 20	34 ± 16	525 ± 23	653 ± 16	−2341 ± 232	563 ± 27	306 ± 21
18B	——	5.4±0.4	17 ± 20	−11 ± 54	599 ± 60	651 ± 54	−384 ± 42	417 ± 32	356 ± 21
21A	15.33 ± 0.03	6.4±0.3	−25 ± 20	−40 ± 21	643 ± 23	679 ± 21	−1410 ± 89	543 ± 29	362 ± 20
21B	15.10 ± 0.05	6.8±0.2	23 ± 17	32 ± 12	429 ± 17	502 ± 12	−1333 ± 232	463 ± 22	250 ± 16
21C	14.82 ± 0.04	5.9±0.4	−47 ± 24	−61 ± 48	670 ± 47	788 ± 48	−572 ± 50	478 ± 36	421 ± 25

Table 2: Parameters of the fitting of Equation 2. Note that neither in E-18B nor in E-21C are blue components, as there is no detection of it and any fit would be over the noise. [a] Studied epochs. [b] AB magnitude range in K band for the corresponding epochs, when possible. [c] EW of the line in the limits exposed in the text. [d] Centre of the double peak (two components). [e] Centre of the whole line considering it as a single Gaussian. [f] FWHM of the double peak (two components). [g] FWHM of the total line considering it as a single Gaussian. [h] Blue edge of the line, computed as three times the standard deviation of the bluest component. [i] Red edge of the line, computed as three times the standard deviation of the reddest component. [j] Separation between the centre of the peaks of the double-peaked component.

similarity between E-18B and E-21C. This is of the highest interest, as the former corresponds to a state close to quiescence consistently with previous works (Koljonen & Hovatta, 2021), while in E-21C is still debated the accretion state. The form of both lines seems to point to a similar origin, at least in the NIR.

From a visual analysis of the fitting, we see that the resulting lines from adding the individual components (solid blue lines) are generally in good agreement with the data. However, the higher noise level in E-18A, E-18B, and E-21C results in a higher uncertainty in the fitting.

It is interesting to compare the fits of the different epochs and their relation with the X-ray luminosity. This project covered three X-ray luminosity epochs: high luminosity in an outburst (E-17), declining luminosity close to quiescence (E-18A and E-18B), and low luminosity with a flare (E-21A, E21B, and E-21C). Considering the previously explained model of a Keplerian disk (Section 1.1.1), it is interesting to study the double peak separation as it gives information about the formation distance of the line to the compact object. In this case, epochs E-18B and E-21C have the two largest double peak separations. It is notable that E-21C shows a higher separation, which could be related to a closer formation of Brγ line to the BH than in the case of E-18B. In this epoch, we observed the lowest X-ray luminosity of all observation campaigns with GTC. In addition to that, E-18B separation is comparable to E-21A. Moreover, the X-ray luminosity in both epochs is also comparable (around 0.3 Photons cm^{-2}s^{-1})[3].

We also see that the blue components in E-17 and E-18A are consistently broader than in E-21A and E-21B, and so are their terminal velocities. It seems to be a correlation between the double peak separation and the blue component center. However, the width of the extra component does not seem to follow a clear pattern. In the case of the double peak profile, their width is much similar, being comparable between E-17 and E-21B, and E-18A and E-21A.

3.2. Photometry

To study the photometrical variation, we used the reduced images resulting from the process of Section 2.2. For each image, we did aperture photometry of four stars (GRS 1915+105, shown in Table 3 and three reference stars, whose bibliographic information is summarized in Table 4, that were used to do differential photometry), using an aperture of 2 times the seeing (previously measured from five to seven punctual objects with `PyRAF` to average). With this, it was possible to have three different AB photometry measures of the source in K_{spec}, and as a test, we also computed the magnitude of each reference star using the others, ensuring that they did not change between nights. If these tests were not consistent, either we considered only the reliable values or we rejected the image. The different observations of the same night were aggregated to increase the SNR. This AB

[3]This is not conclusive, as the lack of measurements in MAXI between MJD 59437 and MJD 59458 limits our knowledge about the source luminosity between both data, which includes E-21A and E-21B.

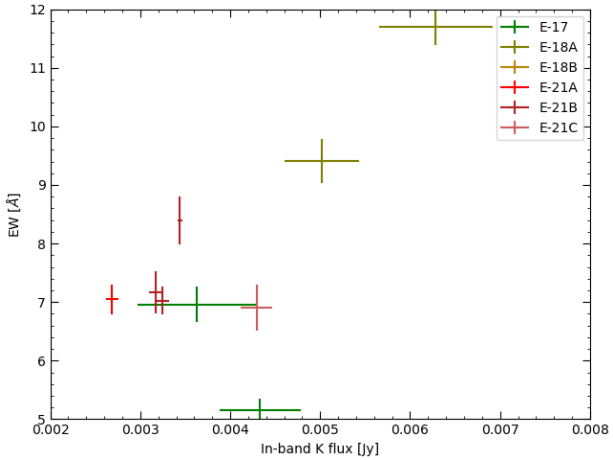

Figure 8: EW against K-band flux (X-axis) on the days when both measurements were available and reliable.

photometry allowed us to get the flux in each observation as

$$f_K = 10^{-m_{\rm AB}/2.5-19.44}\mathrm{erg/s/cm^2/Hz}, \quad (3)$$

where $m_{\rm AB}$ is the magnitude in the AB system.

3.2.1. The equivalent width of Brγ and the NIR flux

In Figure 8, we see the relation between the EW of Brγ against the derived flux from the AB magnitudes. As we can see, there is a clear correlation between the K-flux and the equivalent width, supporting the idea that the greater the NIR flux, the more prominent the line is. This relation is expected for a certain luminosity range (above which the Brγ may saturate) assuming the line is formed in the disk. There are several outliers (from epochs E-17 and E-21C), probably caused by a great contribution from the continuum.

4. Discussion

As we have already commented, the separation between the double peak components depends on the disk radius at which the Brγ emission is formed. In particular, the double peak separation increases when the emission is closer to the compact object. At the same time, the emission radius depends on the physics of the disk. For example, an irradiated disk would have NIR emissions from outer distances than those less irradiated. Consequently, those intrinsically luminous sources are expected to emit Brγ from outer regions of the accretion disk. This would result in a lower separation.

E-17, which corresponds to high X-ray luminosity, displays one of the lowest double peak separations. At the same time, it also shows one of the relatively more remarkable blue excess (with a relative intensity of 37% of the main peak) and the lowest double-peaked intensity when normalized. However, in Figure 8 we see that the corresponding EW does not follow the same tendency as other epochs considering its K band flux. This could be related to an extra continuum contribution without Brγ emissions that would cover the real line strength. A possibility for that would be a higher ionization of this new source. The non-detection of He II (a hydrogen-like atom with higher ionization) is of high interest when interpreting this variation in H I. It could indicate that the reduction in the Brγ intensity would not be related to higher hydrogen ionization. Otherwise, we would expect to start seeing an increase of ionized helium. Nonetheless, this line is typically relatively weak and can be hidden by the continuum when this is too strong (as we have argued above it should be in this case). In conclusion, the non-detection of He II in all epochs suggests a non-important effect of ionized hydrogen to the lower intensity observed, but the high continuum emission makes it difficult to fully reject an ionization effect in the line intensity difference. An origin from out of the disk for this extra NIR continuum is also possible (e.g. in the jet), but no further discussion will be carried out in this work.

At the same time, during the X-ray luminosity decay, E-18B shows innermore line emissions than E-18A. This is consistent with the declining X-ray luminosity and consequent lower irradiation from the central engine, which would result in the cooling of the disk. In fact, the slow decline observed during E-18B and its consistent low luminosity makes it possible to think of a steady low-luminosity more than a linear decay state. We can see that E-18A does not present an important continuum emission compared to its line intensity in the NIR, while no photometry was possible for E-18B.

Finally, we focus on the observed flare at low X-ray luminosity. For both E-21A and E-21B, we do not have MAXI measurements of the X-ray luminosity. In that sense, we can estimate it by interpolation, but a reflare (as the observed few weeks later, between MJD 59455 and 59470) would be possible. However,

we would not expect a luminosity much higher that the previous maximum, considering the evolution. All in all, it may present a significant increase in luminosity. In Brγ, we see an irregular evolution of the double-peaked profile (in E-21A is emitted inner than in E-21B, but E-21C is emitted in the innermost parts) consistent with a non-constant decay of the flare. At the same time, both E-21A and E-21B have a consistent NIR flux, which would support the idea of a lower emission due to less X-ray irradiation. Again, this would point to a reflare during the gap, in which E-21B would have a higher X-ray luminosity than E-21A. The comparative study between epochs points to an important effect of irradiation of high energy in the disk. This would be the reason for the similitude in the double peak separation for E-17B and E-21A, which would be the response to similar X-ray luminosities. For this reason, we can say that E-21C follows the expected behavior for the corresponding X-ray luminosity: its emission is from the innermost disk, consistent with its lowest X-ray luminosity. As in E-17, E-21C does not follow perfectly the same trend in the relation NIR flux-EW as the other epochs. The great variation in double peak separation in the 2021 flare (from 250 km/s in E-21B to 420 km/s in E-21C) does not have any equivalence in the previous campaigns. It may point to a more efficient cooling than in previous epochs, which would allow a faster transition of the Brγ emission to an inner radius.

As we have seen, the Brγ behavior studied in this project for all the six observed epochs is consistently related to the observed X-ray luminosity. Nonetheless, for the year 2021, previous works have argued that a local absorber could be hiding the real X-ray luminosity (see Section 1). The high equivalent column density necessary ($N_{\rm H} \geq 10^{23}{\rm cm}^{-3}$) is an order of magnitude larger than typical extinction values measured in that direction. According to this, the internal obscuration would be the dominant effect in the diminished flux measured. Our observations suggest that this absorber, if present, should be placed inner to the emission region of Brγ for E-21C (the one with the lower emission radius), much closer to the compact object. Otherwise, this line, associated with colder gas, would be emitted further away due to the higher temperature at this distance caused by irradiation. Moreover, this result could not be an observational effect of the absorption, as any absorption affecting Brγ would produce a decrease in the line intensity, but would not have any effect on the separation of the double peak.

The mechanism proposed for this surrounding material, according to Miller et al. (2020), is a failed magnetic wind in the inner part and a cooler component from a thermally driven outflow in the outer part. Nonetheless, we can argue that this high density concentrated in the innermost orbits around the BH seems unlikely. For this reason, we do not support the Seyfert 2 equivalence proposed by Miller et al. (2020), as the obscuration distance is expected to be very low, while in AGN is at larger distances, even considering the mass-scaled version. This argument added to the variation timescales presented in Motta et al. (2021) to refuse this proposal.

Another (simpler) possibility to explain the measured drop in X-ray luminosity is that we are witnessing a real low luminosity state resulting from a reduced accretion rate. This scenario would be similar to the one in E-18B, and would not be new in LMXBs. We have seen that the behavior of E-18B is similar to the one in E-21A, with a similar X-ray luminosity consistent with quiescence. This trend is more clear in the highest double peak separation in E-21C, which is the expected behavior for quiescence with lower X-ray luminosity when considering the physics involved. In conclusion, this scenario of a lower accretion rate seems to be preferred both by its simplicity and its capacity to explain the NIR observations.

4.1. Blue wing excess component

Now we can discuss the nature of the extra blue emission detected in E-17, E-18A, E-21A, and E-21B. Although different origins are possible (mainly two: it could either be an element only observed in emission when it is excited in certain epochs or a signature for a NIR wind), we see a great variation in this excess. The reason for this should be the physics involved in the origin of this component. The blue edge velocities detected, ranging from ~1300 km/s to ~2300 km/s (see Table 3), are consistent with winds in other LMXBs (see Table 2 in Panizo-Espinar et al., 2022, and references therein for a brief overview), which directly points to this cause. This origin would also explain the variation in blue edge velocities among different epochs. Moreover, it would match the cold thermally driven outflow proposed in Miller et al. (2020). Assuming this explana-

tion, we can derive a proxy of the radius at which the mass is lost, R_w. We consider no auto-gravitation of the disk and a mass for the BH of $M_{BH} = 12.4^{+2.0}_{-1.8} M_\odot$ (Section 1). Then, this terminal velocity could be considered as the escape velocity at a given distance from the central object. The simple equation that gives that value is

$$R_w = \frac{2\, M_{BH}\, G}{v_{lim}^2}, \tag{4}$$

where v_{lim} is the terminal velocity of the blue component. The resulting distance is between $\sim 5{\times}10^{10}$ cm-$\sim 2 \times 10^{11}$ cm. This is similar to the wind launching radius derived for other systems such as V404 Cygni (Muñoz-Darias et al., 2016). This means that the wind is not formed close to the BH, but neither in the outermost part of the disk provided its great size.

Considering the mass of the compact object, it results in a gravitational radius, defined as

$$R_G = \frac{2GM}{c^2}, \tag{5}$$

of $R_G = (1.83^{+0.30}_{-0.27}) \times 10^6$cm. Then, the wind origin would be at a distance $\sim 25000 R_g$-$100000 R_g$ of the BH. This distance in gravitational radius indicates this wind does not suffer from important relativistic effects. Following Miller et al. (2020), the bound failed magnetic wind should be interior to this radius, surrounding the innermost part of the engine. This is consistent with the previous qualitative argument (see Section above) and, again, unlikely with great densities.

It is worthy to briefly discuss the non-detection of the extended wing in E-18B and E-21C. Due to the lower SNR in both cases, it is difficult to conclusively reject the idea of a blueshifted component under the noise level. However, its relevance would be reduced and it seems more probable the absence of these winds. This is not surprising, especially if we assume they are thermal-driven winds. In these epochs, considering the low X-ray luminosity, we do not expect strong irradiation from the inner part that would be necessary to produce them.

5. Conclusions

To summarize, in this project we have used NIR spectroscopy of the LMXB GRS 1915+105 during six epochs, covering different X-ray luminosities, to follow up on its evolution during the last five years, including the debated state of the last three years. The detailed study of Brγ line during the different epochs has shown a clear correlation with X-ray luminosities, highlighting the important role of the accretion physics for the spectra of this source.

The analysis carried out in this thesis has also shown the possible presence of NIR winds from the disk in four of the six epochs, including two of the three epochs corresponding to the 2021 flare. The two epochs in which they were not detected corresponded to those close to quiescence in X-ray, marking a possible role of irradiation and the possible thermal origin of the wind. The detection of these outflows was possible thanks to the great inclination of the system.

In the particular case of the flare observed in 2021, the NIR responded to the variability measured in X-ray by MAXI, finishing in a state consistent with quiescence. For this reason, we argued that either the obscured state proposal is not correct or the absorber is located between the X-ray emission and the outer disk. The latter would justify that the NIR emission seems to respond to the same X-ray luminosity that we are measuring.

Nevertheless, we do not reject a certain contribution from the internal obscuration to the luminosity changes. This could be produced by the surrounding material from previous outflows. However, the discussion presented here is robust enough to support the main role of the lower accretion rate in the observed changes. The following proposed explanations for the current state of the source should account for the different observations already available, in radio, X-ray, and now also in NIR.

In the future, it would be interesting to continue observing the source to study the evolution of the disk and see in the trend continues to be consistent with the results of this thesis. GRS 1915+105 is undoubtedly one of the most interesting LMXB known, and continuing its study will allow the scientific community to better understand this type of source and, in particular, the accretion processes it.

Acknowledgements: I am thankful to my supervisors dr. Teo Muñoz-Darias and Javier Sánchez-Sierras for their support and kind introduction to the topic, as well as their constructive comments that have improved this project. This work is partly based on data from the GTC Public Archive at CAB (INTA-CSIC), developed in the framework of the Spanish Virtual Observatory project supported

by the Spanish MINECO through grants AYA 2011-24052 and AYA 2014-55216. The system is maintained by the Data Archive Unit of the CAB (INTA-CSIC). This research also made use of the MAXI data provided by RIKEN, JAXA and the MAXI team. `molly` software developed by Tom Marsh is gratefully acknowledged.

References

Antonucci R., 1993, ARA&A, 31, 473

Athulya M. P., Radhika D., Agrawal V. K., Ravishankar B. T., Naik S., Mandal S., Nandi A., 2022, MNRAS, 510, 3019

Balakrishnan M., Miller J. M., Reynolds M. T., Kammoun E., Zoghbi A., Tetarenko B. E., 2021, ApJ, 909, 41

Begelman M. C., McKee C. F., Shields G. A., 1983, ApJ, 271, 70

Belloni T. M., 2010, in Belloni T., ed., , Vol. 794, Lecture Notes in Physics, Berlin Springer Verlag. p. 53, doi:10.1007/978-3-540-76937-8_3

Belloni T., Méndez M., King A. R., van der Klis M., van Paradijs J., 1997, ApJ, 488, L109

Belloni T., Klein-Wolt M., Méndez M., van der Klis M., van Paradijs J., 2000, A&A, 355, 271

Blanton M. R., Roweis S., 2007, AJ, 133, 734

Brown G. E., Bethe H. A., 1994, ApJ, 423, 659

Burtscher L., et al., 2013, A&A, 558, A149

Castro-Tirado A. J., Brandt S., Lund N., 1992, IAU Circ., 5590, 2

Castro-Tirado A. J., Brandt S., Lund N., Lapshov I., Sunyaev R. A., Shlyapnikov A. A., Guziy S., Pavlenko E. P., 1994, ApJS, 92, 469

Chang E. S., Deming D., 1996, Sol. Phys., 165, 257

Corbel S., Nowak M. A., Fender R. P., Tzioumis A. K., Markoff S., 2003, A&A, 400, 1007

Corral-Santana J. M., Casares J., Muñoz-Darias T., Bauer F. E., Martínez-Pais I. G., Russell D. M., 2016, A&A, 587, A61

Dhawan V., Mirabel I. F., Rodríguez L. F., 2000, ApJ, 543, 373

Done C., Gierliński M., Kubota A., 2007, A&ARv, 15, 1

Dotani T., et al., 1997, ApJ, 485, L87

Eikenberry S. S., Bandyopadhyay R. M., 2000, ApJ, 545, L131

Fender R., Belloni T., 2004, ARA&A, 42, 317

Fender R., Muñoz-Darias T., 2016, in Haardt F., Gorini V., Moschella U., Treves A., Colpi M., eds, , Vol. 905, Lecture Notes in Physics, Berlin Springer Verlag. p. 65, doi:10.1007/978-3-319-19416-5_3

Fender R. P., Garrington S. T., McKay D. J., Muxlow T. W. B., Pooley G. G., Spencer R. E., Stirling A. M., Waltman E. B., 1999, MNRAS, 304, 865

Fender R. P., Belloni T. M., Gallo E., 2004, MNRAS, 355, 1105

Fernández-Ontiveros J. A., Muñoz-Darias T., 2021, MNRAS, 504, 5726

Giacconi R., Gursky H., Paolini F. R., Rossi B. B., 1962, Phys. Rev. Lett., 9, 439

Gilfanov M., 2010, in Belloni T., ed., , Vol. 794, Lecture Notes in Physics, Berlin Springer Verlag. p. 17, doi:10.1007/978-3-540-76937-8_2

Greiner J., Cuby J. G., McCaughrean M. J., Castro-Tirado A. J., Mennickent R. E., 2001, A&A, 373, L37

Hare J., et al., 2020, ApJ, 890, 57

Harmon B. A., Paciesas W. S., Fishman G. J., 1992, IAU Circ., 5619, 2

Harmon B. A., Deal K. J., Paciesas W. S., Zhang S. N., Robinson C. R., Gerard E., Rodríguez L. F., Mirabel I. F., 1997, ApJ, 477, L85

Hettinger T., Badenes C., Strader J., Bickerton S. J., Beers T. C., 2015, ApJ, 806, L2

Homan J., Neilsen J., Steiner J., Remillard R., Altamirano D., Gendreau K., Arzoumanian Z., 2019a, The Astronomer's Telegram, 12742, 1

Homan J., Neilsen J., Gendreau K., Arzoumanian Z., Remillard R., Steiner J., Altamirano D., Wolff M. T., 2019b, The Astronomer's Telegram, 13308, 1

Iwakiri W., et al., 2019a, The Astronomer's Telegram, 12761, 1

Iwakiri W., et al., 2019b, The Astronomer's Telegram, 12787, 1

Kalogera V., Baym G., 1996, ApJ, 470, L61

Kausch W., et al., 2015, A&A, 576, A78

Klein-Wolt M., Fender R. P., Pooley G. G., Belloni T., Migliari S., Morgan E. H., van der Klis M., 2002, MNRAS, 331, 745

Koljonen K. I. I., Hovatta T., 2021, A&A, 647, A173

Koljonen K. I. I., Tomsick J. A., 2020, A&A, 639, A13

Liu B. F., Taam R. E., 2009, ApJ, 707, 233

Longair M. S., 1994, High energy astrophysics. Vol.2: Stars, the galaxy and the interstellar medium. Vol. 2

Martynov D. Y., 1971, Course of general astrophysics. Text-book for students of astronomy.

Matsuoka M., et al., 2009, PASJ, 61, 999

Michell J., 1784, Philosophical Transactions of the Royal Society of London Series I, 74, 35

Miller J. M., et al., 2020, ApJ, 904, 30

Mirabel I. F., Rodríguez L. F., 1994, Nature, 371, 46

Mirabel I. F., Rodriguez L. F., Marti J., Teyssier R., Paul J., Auriere M., 1993a, IAU Circ., 5773, 2

Mirabel I. F., et al., 1993b, IAU Circ., 5830, 1

Miyamoto S., Kitamoto S., Iga S., Negoro H., Terada K., 1992, ApJ, 391, L21

Miyamoto S., Iga S., Kitamoto S., Kamado Y., 1993, ApJ, 403, L39

Miyamoto S., Kitamoto S., Hayashida K., Egoshi W., 1995, ApJ, 442, L13

Motta S. E., et al., 2021, MNRAS, 503, 152

Muñoz-Darias T., Coriat M., Plant D. S., Ponti G., Fender R. P., Dunn R. J. H., 2013, MNRAS, 432, 1330

Muñoz-Darias T., et al., 2016, Nature, 534, 75

Muñoz-Darias T., et al., 2020, ApJ, 893, L19

Narayan R., Yi I., 1995, ApJ, 452, 710

Negoro H., et al., 2018, The Astronomer's Telegram, 11828, 1

Neilsen J., Lee J. C., 2009, Nature, 458, 481

Neilsen J., Remillard R. A., Lee J. C., 2011, ApJ, 737, 69

Neilsen J., Homan J., Steiner J. F., Marcel G., Cackett E., Remillard R. A., Gendreau K., 2020, ApJ, 902, 152

Oppenheimer J. R., Volkoff G. M., 1939, Physical Review, 55, 374

Panizo-Espinar G., et al., 2022, arXiv e-prints, p. arXiv:2205.09128

Ponti G., Fender R. P., Begelman M. C., Dunn R. J. H., Neilsen J., Coriat M., 2012, MNRAS, 422, L11

Psaltis D., 2008, Living Reviews in Relativity, 11, 9

Reid M. J., McClintock J. E., Steiner J. F., Steeghs D., Remillard R. A., Dhawan V., Narayan R., 2014, ApJ, 796, 2

Sana H., et al., 2012, Science, 337, 444

Seyfert C. K., 1943, ApJ, 97, 28

Shakura N. I., Sunyaev R. A., 1973, A&A, 24, 337

Shapiro S. L., Teukolsky S. A., 1986, Black Holes, White Dwarfs and Neutron Stars: The Physics of Compact Objects

Smak J., 1969, Acta Astron., 19, 155

Smette A., et al., 2015, A&A, 576, A77

Steeghs D., McClintock J. E., Parsons S. G., Reid M. J., Littlefair S., Dhillon V. S., 2013, ApJ, 768, 185

Taam R. E., Chen X., Swank J. H., 1997, ApJ, 485, L83

Tananbaum H., Gursky H., Kellogg E. M., Levinson R., Schreier E., Giacconi R., 1972, ApJ, 174, L143

Tolman R. C., 1939, Physical Review, 55, 364

Trushkin S. A., Nizhelskij N. A., Tsybulev P. G., Bursov N. N., Shevchenko A. V., 2019, The Astronomer's Telegram, 13304, 1

Truss M., Done C., 2006, MNRAS, 368, L25

Walton D. J., et al., 2017, ApJ, 839, 110

Yungelson L. R., Lasota J. P., Nelemans G., Dubus G., van den Heuvel E. P. J., Dewi J., Portegies Zwart S., 2006, A&A, 454, 559

Ziółkowski J., Zdziarski A. A., 2017, MNRAS, 469, 3315

van den Heuvel E. P. J., 1992, Endpoints of stellar evolution: the incidence of stellar mass black holes in the Galaxy., In ESA, Environment Observation and Climate Modelling Through International Space Projects. Space Sciences with Particular Emphasis on High-Energy Astrophysics p 29-36 (SEE N93-23878 08-88)

Appendix

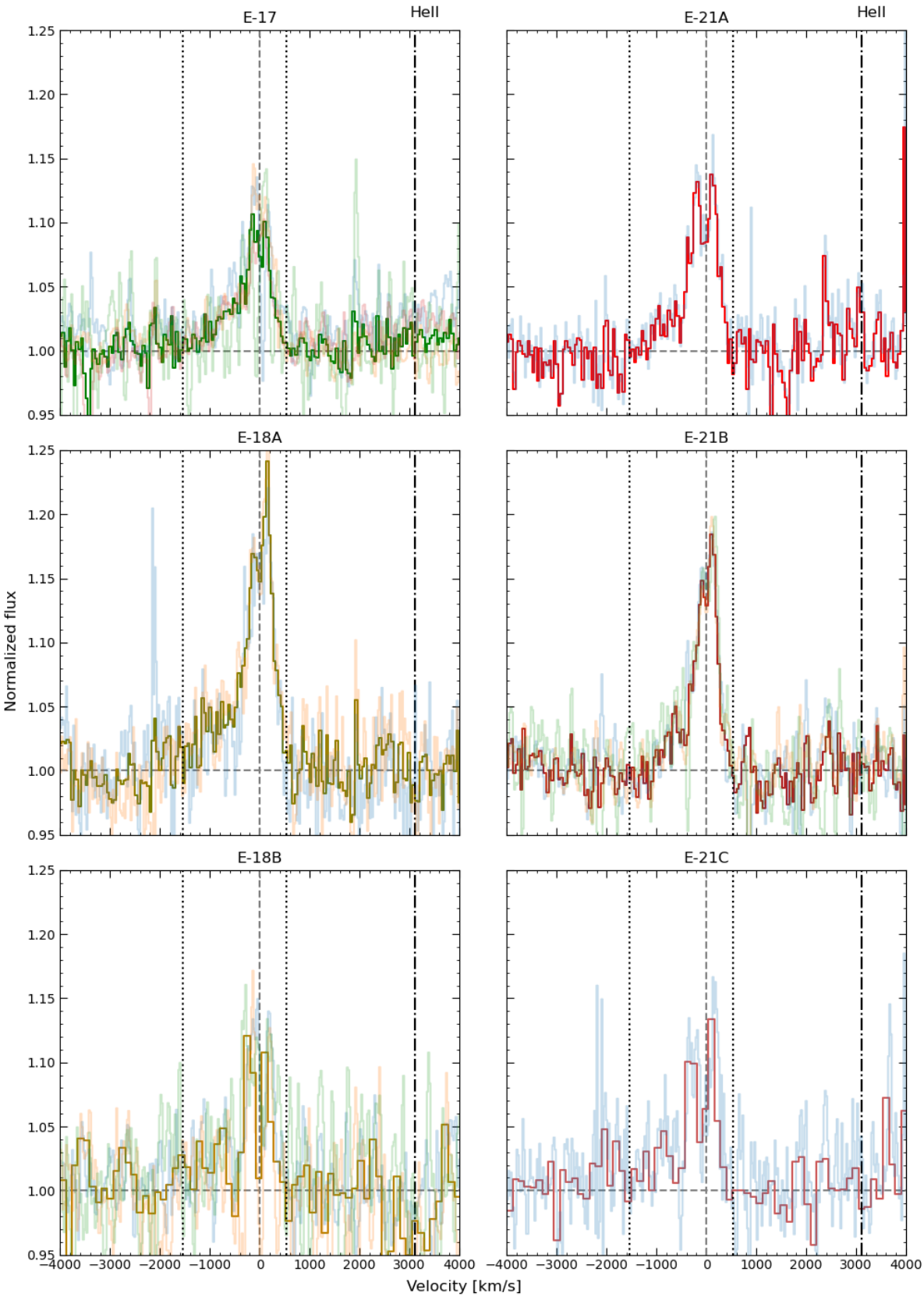

Figure 9: Average spectra of the corresponding epochs over the individual spectra they are composed of (more transparent). The dotted vertical lines correspond to the integration limits to compute the Equivalent Width. Additionally, the dash-dot lines around 3000 km/s mark the expected position for the He II lines. Note the non-detection of this line in any of the spectra.

Epoch[(a)]	μ_b [km/s][(b)]	μ_1 [km/s][(c)]	μ_2 [km/s][(d)]	σ [km/s][(e)]	σ_b [km/s][(f)]	Analytical limit [km/s][(g)]	Double peak separation [km/s][(h)]
17	-492 ± 186	-108 ± 15	170 ± 15	109 ± 9	477 ± 77	$-1921 \pm 297, 498 \pm 32$	278.0 ± 21.1
18A	-648 ± 164	-127 ± 17	179 ± 10	128 ± 8	564 ± 55	$-2341 \pm 232, 563 \pm 27$	305.7 ± 20.4
18B	——	-161 ± 13	195 ± 15	74 ± 9	——	$-384 \pm 42, 417 \pm 32$	356.0 ± 20.4
21A	-860 ± 68	-206 ± 14	156 ± 14	129 ± 9	183 ± 19	$-1410 \pm 89, 543 \pm 29$	362.1 ± 19.7
21B	-480 ± 214	-102 ± 14	147 ± 9	105 ± 7	284 ± 30	$-1333 \pm 232, 463 \pm 22$	249.8 ± 16.3
21C	——	-257 ± 18	163 ± 16	105 ± 10	——	$-572 \pm 50, 478 \pm 36$	420.5 ± 24.4

Table 3: Parameters of the fitting of Equation 2. Note that neither in 18B nor in 21C are blue components, as there is no detection of it and any fit would be over the noise. [(a)]Epoch of the fitted line. [(b)]Central value of the blue wing. [(c)]Central value of the blue peak of the line. [(d)]Central value of the red peak of the line. [(e)]Standard deviation of the central peaks. [(f)]Standard deviation of the blue wing. [(g)]Limit of the line, corresponding to the central value of their bluest component minus three times the standard deviation of it, and the central value of the reddest component plus three times the standard deviation of the same. [(h)]Separation between the double peaks.

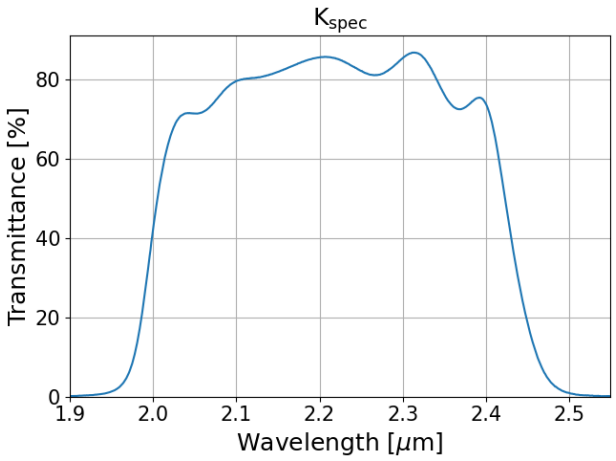

Figure 10: Transmittance of the K_{spec} filter from EMIR.

RA[(a)]	Dec[(b)]	K_{spec} magnitude[(c)]
19:15:10.73	10:57:18.1	13.78 ± 0.06
19:15:13.13	10:57:00.0	13.20 ± 0.05
19:15:14.30	10:56:07.9	12.68 ± 0.03

Table 4: Photometry of the three reference stars used to do differential photometry of GRS 1915+105. [(a)]Right Ascension. [(b)]Declination. [(c)]Magnitude in K_{spec} band of the reference stars measured by the 2MASS mission. Note that these values are in the Vega system. To convert to the AB system desired here, we used that $m_{AB} - m_{Vega} = 1.85$ derived for K_{spec} band in Blanton & Roweis (2007).